Probing magnetic ordering in air stable iron-rich van der Waals minerals

Muhammad Zubair Khan[1,], Oleg E. Peil[2], Apoorva Sharma[3], Oleksandr Selyshchev[3,6], Sergio Valencia[4], Florian Kronast[4], Maik Zimmermann[5], Muhammad Awais Aslam[1], Johann G. Raith[5], Christian Teichert[1], Dietrich R.T. Zahn[3,6], Georgeta Salvan[3,6], and Aleksandar Matković[1,*]*

[1] Chair of Physics, Department Physics, Mechanics and Electrical engineering, Montanuniversität Leoben, 8700, Leoben, Austria.

[2] Materials Center Leoben Forschung GmbH (MCL), 8700, Leoben, Austria.

[3] Semiconductor Physics, Chemnitz University of Technology, D-09107, Chemnitz, Germany.

[4] Department of Spin and Topology in Quantum Materials, Helmholtz-Zentrum Berlin, Albert-Einstein-Str. 15, D-12489, Berlin, Germany.

[5] Chair of Resource Mineralogy, Montanuniversität Leoben, 8700, Leoben, Austria.

[6] Centre for Materials, Architecture, and Integration of Nanomembranes (MAIN), Chemnitz University of Technology, 09126, Chemnitz, Germany.

Corresponding email: muhammad.khan@unileoben.ac.at, aleksandar.matkovic@unileoben.ac.at

Keywords: 2D magnetic insulators, layered magnetic minerals, Fe-rich phyllosilicates

Abstract

In the rapidly expanding field of two-dimensional materials, magnetic monolayers show great promise for the future applications in nanoelectronics, data storage, and sensing. The research in intrinsically magnetic two-dimensional materials mainly focuses on synthetic iodide and telluride based compounds, which inherently suffer from the lack of ambient stability. So far, naturally occurring layered magnetic materials have been vastly overlooked. These minerals offer a unique opportunity to explore air-stable complex layered systems with high concentration of local moment bearing ions.

We demonstrate magnetic ordering in iron-rich two-dimensional phyllosilicates, focusing on mineral species of minnesotaite, annite, and biotite. These are naturally occurring van der Waals magnetic materials which integrate local moment baring ions of iron via magnesium/aluminium substitution in their octahedral sites. Due to self-inherent capping by silicate/aluminate tetrahedral groups, ultra-thin layers are air-stable. Chemical characterization, quantitative elemental analysis, and iron oxidation states were determined via Raman spectroscopy, wavelength disperse X-ray spectroscopy, X-ray absorption spectroscopy, and X-ray photoelectron spectroscopy. Superconducting quantum interference device magnetometry measurements were performed to examine the magnetic ordering. These layered materials exhibit paramagnetic or superparamagnetic characteristics at room temperature. At low temperature ferrimagnetic or antiferromagnetic ordering occurs, with the critical ordering temperature of 38.7 K for minnesotaite, 36.1 K for annite, and 4.9 K for biotite. In-field magnetic force microscopy on iron bearing phyllosilicates confirmed the paramagnetic response at room temperature, present down to monolayers. Our results unveil a new class of magnetic insulators with ambient stability, which enable up to 100 percent substitution of the core ions with the magnetic moment baring species.

1 Introduction:

The discovery of graphene[1] sparked the development of many other two-dimensional (2D) van der Waals (vdW) materials.[2] Driven by the needs in spintronics[3,4] magnetism was induced in intrinsically non-magnetic 2D materials[5] via defects,[6,7] topology,[8] and doping.[9,10] Moreover during the recent years a broad range of layered intrinsic magnetic compounds has been investigated in the search of persistent magnetic response at the 2D limit.[11–13] Monolayers of $FePS_3$,[14] CrI_3,[15] $Cr_2Ge_2Te_6$,[16] and Fe_3GeTe_2[17] are some of the most studied 2D magnetic systems thus far. Interesting enough, the magnetic state of these systems can be controlled by means of electric fields. Magnetoelectric coupling opens the door for the design of 2D magnetic material-based devices for electrically coupled spintronics.[18–20] Further potential ways to control magnetic devices are interface-based spin-transfer torque[21] and voltage controlled magnetic anisotropy.[22] Magnetic anisotropy is the key requisite for perceiving 2D magnetism.[23] Generally, magnetic properties of solid materials depend on the spin orbit coupling and exchange interaction.[24] The reciprocity among exchange interaction, spin orbit coupling, and Zeeman effect describes the orbital moment, magneto crystalline anisotropy, and the ramifications of external magnetic fields.[25] The magnetocrystalline anisotropy and the spin Hamiltonian, being material dependent can be

altered by strain engineering[26] and optical tuning.[27,28] Furthermore, tuning the twist angle between bilayers of a 2D homo system enables the possibility to alter the interlayer exchange interaction and controlling the spin degree of freedom in 2D magnetic materials.[29]

For device applications, 2D magnetic materials enable atomically sharp interfaces and the preservation of long-range magnetic ordering down to their mono-layers.[30] However, ambient stability is a limiting factor for their integration into future technologies. One of the possible approaches to overcome this hurdle, is introducing small quantities of V,[31] Fe,[32] or Co[33,34] in transition metal dichalcogenide monolayers via substitution of the transition metal ions. Such type of diluted magnetic semiconductor mono-layers are air stable and exhibit ferromagnetic ordering at room temperature.[31–35] In these systems, controlled dopant concentration and their dilution in the host 2D semiconductor matrix are the key factors.[36]

In contrast to the above-mentioned synthetic 2D systems, there is a variety of vdW minerals[37–41] naturally occurring bulk layered crystals which offer a wide range of structural and compositional variations.[42–47] However, besides natural graphite and molybdenite most of the other explored 2D materials are obtained from synthetic sources, while the properties of naturally occurring vdW species remain mostly unexplored.[37,48] One of the first natural 2D phyllosilicates to be employed in electronics and nanomechanics was talc.[49–52] Recently, mica group members started attracting attention as multifunctional insulators in 2D electronic applications,[42,53,54] and especially in novel memory concepts with 2D semiconductors.[55,56] As for the magnetic vdW minerals, the naturally occurring sulfosalt cylindrite with vdW superlattice was explored.[57] While it is possible to exfoliate monolayers, the bulk antiferromagnetic Néel temperature (T_N) was found to be below 20 K.[57] Furthermore, a recent study has demonstrated the possibility to exchange interlayer ions in micas and vermiculites and to fabricate twistronic superlattices, causing interlayer species to reorder accordingly with the twisting angle via the stacking method.[58] Bulk iron (Fe)-rich phyllosilicates – such as minnesotaite and annite – were reported to have an in-plane easy axis, commonly exhibiting layered antiferromagnetism.[59] Thus far, these materials were not explored at the 2D limit. Furthermore, synthetic crystals of flurophlogopite mica were demonstrated to exhibit strong paramagnetic response at low temperatures.[60] We have reported the first observation of weak ferromagnetism in naturally occurring Fe-rich talc at room temperature, confirming that the magnetic response remains down to the monolayer, and that even monolayers are fully air stable.[61]

In this article, we explore minnesotaite, annite, and biotite, as iron-rich members of the phyllosilicate family. These layered systems are inherently magnetic, fully stable under ambient conditions, and can be thinned down to ultra-thin films, and monolayers with the same mechanical cleavage methods as applied for the other 2D materials.[1] They integrate local moment bearing ions of Fe via magnesium (Mg) or aluminium (Al) substitution in their octahedral sites, with substitution ratios of up to 100% with respect to the iron-free species of talc and phlogopite. Due to self-inherent capping by silicate/aluminate tetrahedral groups, the monolayers are air-stable. These minerals exhibit strong paramagnetic behaviour at room temperature and order ferrimagnetically or antiferromagnetically below the critical ordering temperature. We provide correlations between the iron concentration, layer structure, iron oxidation states, and their magnetic response. Furthermore, we discuss the possibilities to tune the structure of magnetic phyllosilicates in order to achieve higher critical ordering temperatures. Our study of 2D materials obtained by mechanical exfoliation of naturally occurring layered magnetic materials may initiate the development for controllable synthesis of the magnetic phyllosilicates with tailored properties.

2   Results and discussion

2.1. Mineral specimens, layer structure, and exfoliated ultra-thin films of iron-rich phyllosilicates.

Phyllosilicates of interest belong to the class of 2:1 layered minerals composed of two-dimensional sheets of M-(O,OH) octahedra sandwiched between two inward pointing sheets of linked T-O tetrahedra. Cations in the M site are mostly Mg, Al and Fe, while the T sites are occupied by Si and Al.(see Figures 1a-d). They are located at the central octahedral sheets with connection to four O and two adjacent OH groups. In talc, the main M cation is Mg. In some cases, the octahedral sites are also occupied by Fe, cobalt (Co), or nickel (Ni) via cationic substitution,[62] e.g. for Fe-substituted talc, the substitution ratio (η) can be expressed as $\eta = N_{Fe}/(N_{Fe} + N_{Mg})$, considering that the only option for the Fe incorporation is the substitution of the central Mg ion. Two major differences of micas in comparison
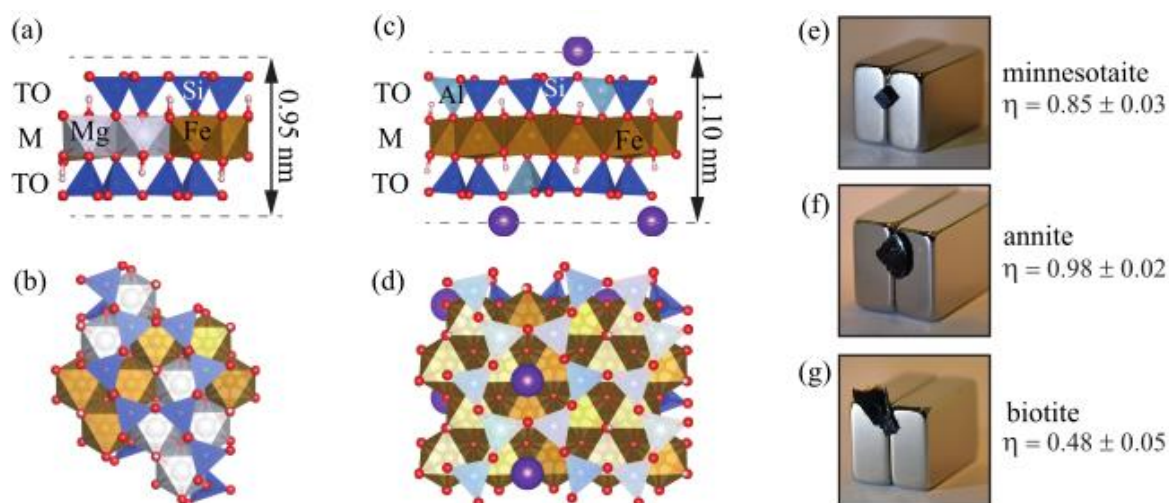
Figure 1: Side (a,c) and top (b,d) views of Fe-substituted talc - minnesotaite (a,b), and Fe-substituted mica – annite (c,d). The structure of biotite is not shown as it resembles the annite structure with lower Fe concentration. Presented are relaxed structures obtained from *ab initio* calculations. The octahedral units with substituted Fe are indicated by orange colour, and Mg containing octahedrals are shown in grey. The interlayer species (K) are represented as purple spheres, Si and Al tetrahedral groups are shown in dark and light blue, respectively. The H and O atoms are denoted as white and red spheres. (e-g) photographs of the examined mineral specimens of minnesotaite, annite, and biotite, with their Fe substitution ratio (η) indicated. The minerals are clinging to a side between two permanent magnets (height of the magnets ~2 cm). Note that as they are (super) paramagnetic at room temperature, the specimens are attracted to the strongest field gradient (*i.e.* between the two opposing poled magnets).

to talc group minerals are the presence of AlO_4 tetrahedral groups in the silicate double layer (with the ratio of Al to Si atoms being close to 1:3) and of larger ionic radius interlayer species (mainly K,Na) located between the 2:1 sheets. The role of the latter is to keep the structure stoichiometry neutral by donating one electron and compensating for the electron deficit created by Al^{3+} ions replacing Si^{4+} ions.[46,63]

Dark coloured mica is commonly referred to as biotite by geologists. Mineralogically, it corresponds to a group of dark micas including the species (endmembers) phlogopite, siderophyllite, annite and eastonite. Phlogopite and annite do not incorporate Al in the M site. In eastonite and siderophyllite additional Al substitutes for (Mg, Fe) balanced by Al for Si in tetrahedral sites (Tschermak's substitution). In most natural biotites there is considerable substitution of this type.[64]

The structural characteristics of talc group minerals and micas are mainly determined by the composition of the octahedral sheet and the fraction of Al^{3+} tetrahedra. For simplicity, we assume that talc contains no Al at all, while the fraction of Al^{3+} ions in trioctahedral micas like annite corresponds to exactly 1/4 of the total number of the tetrahedral groups.[65] In this case, the main variables relevant for talc are η (the fraction of octahedral sites occupied by Fe), and an about 0.15 nm smaller layer separation in the case of talc members due to the lack of the interlayer ions.[49,66] Considering the relaxed structures of both Fe-rich talc and mica, Fe ions should be in a valence state of Fe^{2+}, as this is energetically more favoured over the Fe^{3+} state.[61,65] However, in the particular case of minnesotaite, rather rigid tetrahedral silicate groups do not allow for strain relaxation upon the substitution of Fe in the central site. Consequently, a complex modulated layer structure was proposed to occur.[67] This is supported by our observations of the typical flake morphologies, as mechanical exfoliation yielded elongated multilayer flakes and in general a much lower degree of cleavage than with the samples of annite and biotite. In the case of micas, a fraction of the aluminate tetrahedral groups allows for more flexibility and the monolayers can have up to 100 % of the central site substitution without compromising the layered structure. In general, structural defects, vacancies, and reconstructions due to strain can promote a significant fraction of Fe^{3+} ions in the central octahedral site.[68]
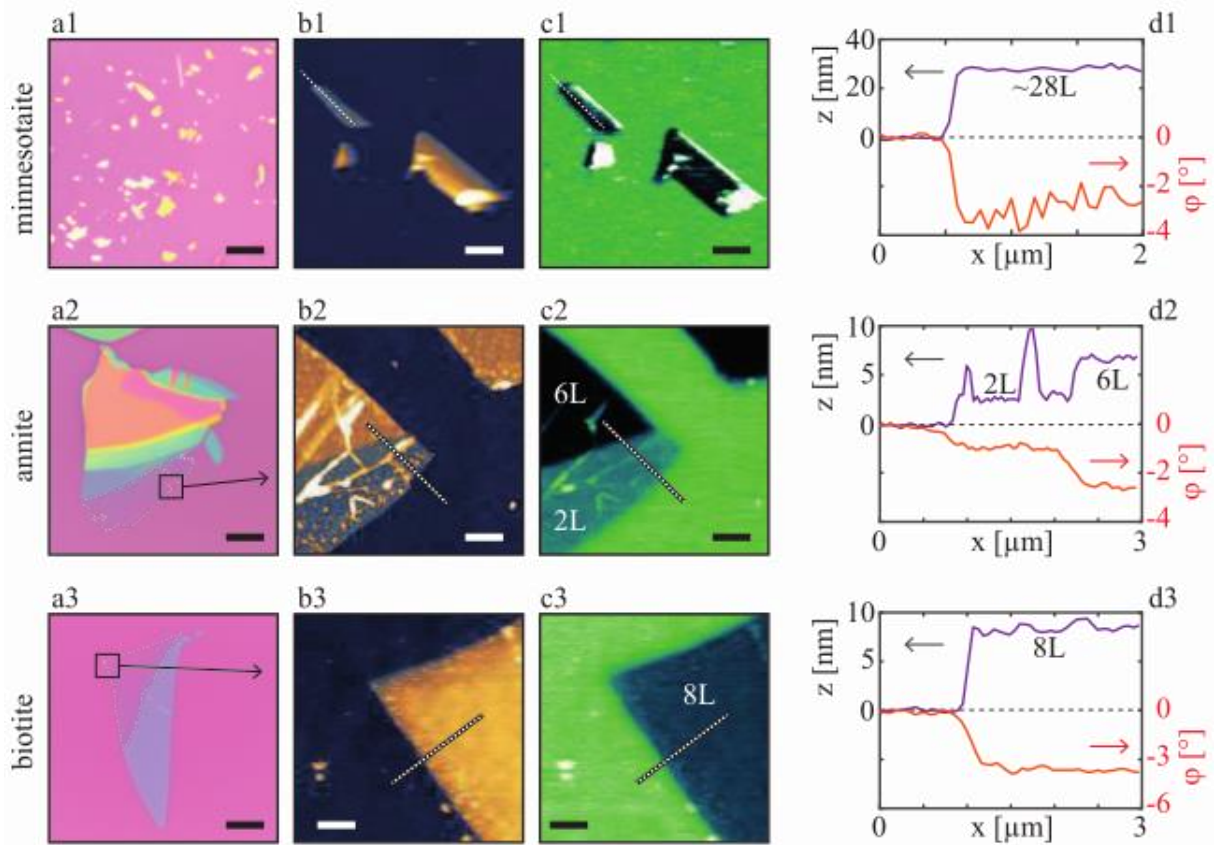
Figure 2: (a1-a3) optical micrographs (60×60 µm², scale bar 10 µm) of exfoliated minnesotaite, annite, and biotite flakes, respectively. Dashed lines in (a2) and (a3) highlight the thin flake regions and the solid squares mark the areas from which the AFM micrographs are presented. (b1-b3) AFM topography images of the exfoliated flakes (6×6 µm², scale bar 1 µm, z-scales 100 nm, 15 nm, and 15 nm respectively). (c1-c3) second-pass phase lag in 180 mT out-of-plane external field, of the same flake areas as in (b1-b3). (d1-d3) presents flake height (left y scale) and MFM phase lag (right y scale) cross-sections, taken perpendicular to the flake's edges. Single lines are presented without line averaging. The cross-sections are indicated in (b1-b3 and c1-c3) by dotted white lines.

Figures 1a-d depict the 3D representation (side and top views of the relaxed structures obtained by *ab initio* calculations) of Fe-substituted talc and mica monolayers. Photographs of the three mineral specimens used in the study (sticking to the side of the permanent magnets) are shown in Figure 1e-g. The chemical composition of all the samples was determined using quantitative electron probe micro analysis -wavelength dispersive X-ray spectroscopy (EPMA-WDS) and X-ray photoelectron spectroscopy (XPS). The examined minnesotaite crystals were obtained from the mineral collection of the University of Minnesota (sample number 14508). The mineral aggregate consists of small crystalline grains of minnesotaite (up to 100 µm in size) with occasional pure talc flakes and SiO_2 inclusions. Based on the systematic Raman spectra taken from the mineral and numerous WDS measurements, we estimate that above 95 % of the grains belong to minnesotaite. The examined minnesotaite samples have $\eta = (0.85 \pm 0.03)$. The empirical formula calculated from EPMA-WDS analyses on the basis of 11 oxygen equivalents per formula unit is $(Fe_{2.5}Mg_{0.5})Si_{4.4}O_{10}(OH)_2$. The detected slight excess of Si could be related to SiO_2 inclusions between minnesotaite grains and to residues of the poly-dimethylsiloxane (PDMS) films used in sample preparation for the WDS experiments (see also methods section).

The examined specimen of annite was obtained from the mineral collection of the Royal Ontario Museum (specimen number M42126.1). The bulk sample is a single-crystal (about 8 mm in diameter). Inclusions of other species were not detected. The empirical formula, determined by WDS, is: $K_{1.02}(Mg_{0.05}Fe_{2.94})Al_{0.94}Si_{3.28}O_{10}(OH)_2$. Iron was found to occupy almost 100 % of the central octahedral sites; $\eta = (0.98 \pm 0.02)$. In both cases of annite and biotite samples, the detected amount of Si (about 6-8 %) can be assigned to PDMS residues, which have been also observed on the crystal graphite support used in WDS experiments.

The examined sample of biotite was obtained from the mineral collection of the Chair of Resource Minerology at the Montanuniversität Leoben (sample number: 9127). The mineral is a single-crystal (about 10 mm in diameter), and inclusions of other species were not detected. The empirical formula (assuming no central octahedral ion vacancies) is: $K_{0.82}(Mg_{1.02}Fe_{1.42}Al_{0.54})(Al_{0.96}Si_{3.23})O_{10}(OH)_2$, as determined by WDS. In the specimen, $\eta = (0.48 \pm 0.05)$ was found. Considering that only Fe and Mg occupy the central octahedral site, the Al amount would be in excess. Therefore, Al ions are likely to occupy about 18 % of the octahedral sites.[69] The observed deficit in the interlayer K ions could lead to incorporation of about 15 % of Fe^{3+} with respect to the total number of Fe ions. However, as seen later in the text, this is not sufficient to explain the observed Fe^{2+}/Fe^{3+} ratio, indicating a more complex relation between the iron oxidation state and the structural defects.

Monolayer and multilayer 2D flakes of minnesotaite, annite, and biotite were prepared from the bulk mineral specimens via micromechanical exfoliation[1] and transferred primarily onto Si/SiO_2 chips (300 nm oxide layer), see Figure 2(a1-a3). All these vdW materials are dielectrics with a band gap of approximately 5-6 eV.[56] Hence, the exfoliated flakes have the issues related to the optical contrast in the visible similar to hexagonal boron nitride.[44,49,70–72] Owing to the high-crystallinity of the starting mineral specimens, high-quality annite and biotite flakes were obtained with large uniform areas (over 30 μm in diameter), and terraces with thicknesses down to few layers. For minnesotaite flakes, due to polycrystallinity of the bulk that likely results from the reconstruction of the crystal structure due to high Fe substitution, cleavage is less pronounced and predominantly elongated multi-layer flakes in form of sticks were observed,[67] as shown in Figure 2(a1-c1). Typical morphologies of the thin flakes of annite and biotite are depicted by the atomic force microscopy (AFM) topography images in Figure 2(b1-b3).

To map the local magnetic response of the flakes, two-pass magnetic force microscopy (MFM) measurements were carried out in the presence of an externally applied out-of-plane magnetic field of 180 mT. Figures 2(c1-c3) present the MFM second pass phase lag images that correspond to the in-field local magnetic response at room temperature. As the samples are superparamagnetic/paramagnetic at room temperature, the external out-of-plane magnetic field is stronger above the flakes in comparison to the surrounding weakly diamagnetic Si/SiO_2 support. Consequently, the magnetized probe is pulled stronger to the surface, yielding a negative contrast with respect to the substrate.[61] A comparison between the topography and the MFM phase lag is provided by their cross-sections in Figure 2(d1-d3). A correlation between the height and the second pass phase lag were observed, as illustrated for annite where a bi-layer (2L) to six-layer (6L) flake step is presented in Figure 2(b2-d2). The magnetic behaviour is strongly dependent on the amount of Fe ions substituting Mg ions in the octahedral sheet. Moreover, since all other bonds are saturated, Fe ions can take on both 2+ and 3+ valence states as a result of structural variations. As will be shown below, the fraction of Fe^{3+} ions can be significant and their presence makes a strong impact on magnetic properties of phyllosilicates.

To verify the structure and to confirm that the crystallinity is preserved upon mechanical exfoliation, thin flakes of minnesotaite, annite, and biotite were measured by micro-Raman spectroscopy, and their spectral features were analysed with respect to Fe incorporation into the phyllosilicate matrices. For these measurements, thin flakes (between 20 nm and 200 nm) were transferred onto the surface of highly oriented pyrolytic graphite (HOPG).[73] HOPG as a substrate provides good heat dissipation and allows for the long accumulation time needed in order to resolve the spectral features of ultra-thin phyllosilicate flakes. In addition, the vibrational modes of HOPG do not overlap with neither low- nor high-frequency modes of the examined phyllosilicates, which is not the case for SiO_2/Si support. Figure 3 represents the Raman spectra with fundamental and OH associated vibrations for each of the phyllosilicates along with the optical images of the measured thin flakes.

Mostly Raman features of phyllosilicates are predominantly observed in the two spectral ranges: from 250-1200 cm^{-1} and 3000-3800 cm^{-1}. The Raman peaks in the spectral range below 600 cm^{-1} are an indication of the complex set of translational motion of cations in the octahedral site, followed by the peaks between 600-800 cm^{-1} related to the fundamental vibrations ($Si - O_b - Si$).[74] The Raman peaks in the spectral range of 800-1150 cm^{-1} results from the stretching mode of Si and non-bridging oxygen.[74] The peaks from the stretching mode of OH groups in the octahedral sites and potential intercalated H_2O can be observed in the spectral range of 3000-3800 cm^{-1}. In phyllosilicates, the peak positions of the characteristic OH vibrations depend on the difference in the effective ionic radii among Fe^{2+} (0.78 Å), Mg^{2+}(0.72 Å), Fe^{3+}(0.645 Å), and Al^{3+}(0.53 Å).
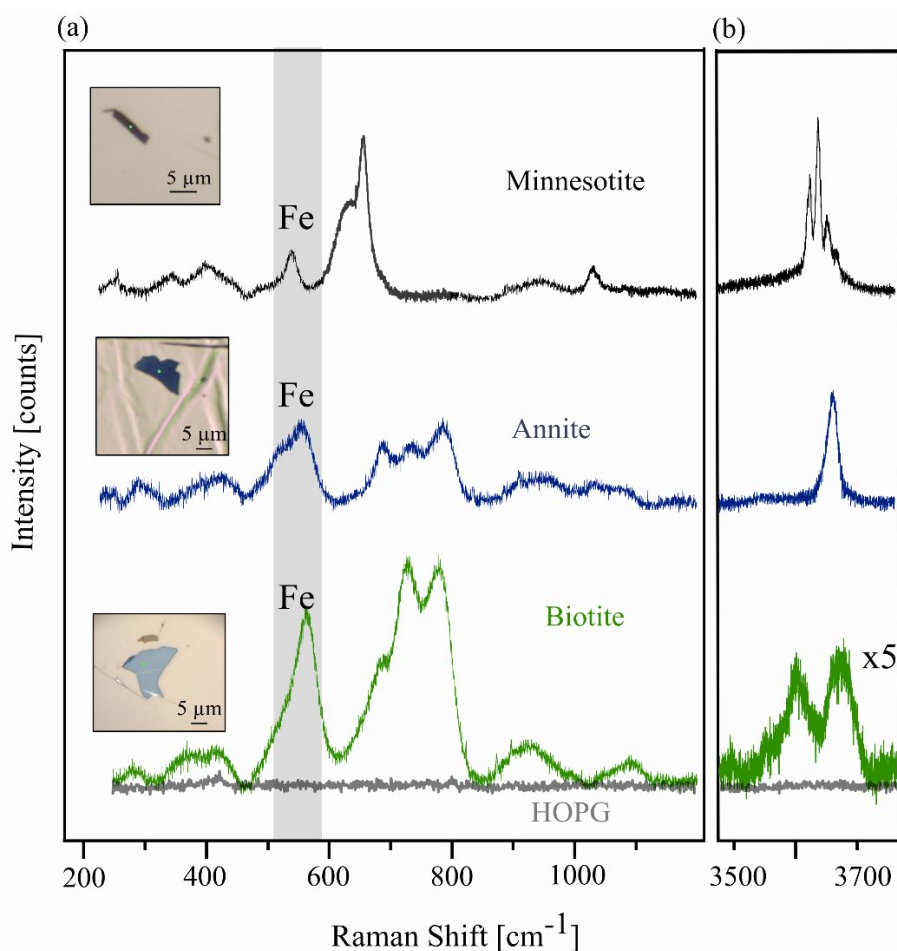
Figure 3: Raman spectra of thin Fe-rich phyllosilicates, showing the fundamental vibrations (a) (250-1200 cm^{-1} range), and the OH vibrations (b) (3500-3700 cm^{-1} range). Top-down, the spectra correspond to minnesotaite, annite, and biotite respectively. Insets present optical micrographs of the flakes on HOPG, from which the measurements were taken, and the green dot indicates the laser positioning. The background spectrum of graphite is shown together with the spectrum of biotite.

Different spectral changes were observed in the case of minnesotaite, annite and biotite, depending on their structural difference and the variation of Fe concentration in the mineral. Figure 3a shows the Raman spectra of fundamental vibrations for all three minerals in the spectral region: 200-1150 cm^{-1}. Raman spectra exhibit the presence of Si-O-Si vibration modes followed by the Fe-O vibration modes in the spectral range of 250-500 cm^{-1} and 500-600 cm^{-1} respectively. In the case of annite and biotite the triplet of peaks between 700-820 cm^{-1} is assigned to the octahedral-tetrahedral bridging oxygen vibration mode,[74] which is observed in the Raman spectra of minnesotaite as a doublet at lower frequencies (600-720 cm^{-1}), as a result of the absence of Al in the minnesotaite structure.

Figure 3b shows the Raman spectra of minnesotaite, annite and biotite in the hydroxyl stretching region. In comparison to talc,[61,74] minnesotaite exhibits major spectral differences due to the substitution of Fe in the octahedral sites. The downshift of peak positions are attributed to the mass effect.[74] A complex OH feature was observed with the three major peaks at 3655, 3626 and 3639 cm^{-1}. These different vibrational modes relate to the presence of Fe^{2+}, Fe^{3+} and Mg^{2+} in the octahedral sites forming $[Fe^{2+/3+}O_4(OH)_2]$ and $[Mg^{2+}O_4(OH)_2]$. In the case of annite and biotite, a strong peak at 3670 cm^{-1} and a doublet peak at 3640 and 3680 cm^{-1} was observed respectively. The splitting in the peaks of biotite is related to the diverse occupancy of Fe, Al and Mg ions at octahedral sites,[75] which is further supported by the presence of single peak for annite, containing 100 % Fe in the octahedral site. Furthermore, in the case of biotite the broadening of OH modes suggest a significant degree of disorder present in the cation sublattice of the octahedral sheet. As discussed below, the presence of the aluminate tetrahedral groups enables both biotite and annite to incorporate higher fractions of Fe^{2+} and Fe^{3+} ions while maintaining the same structure. This is not the case for the talc family members such as minnesotaite.

Therefore, the difference between Fe^{2+} and Fe^{3+} ions in the octahedral groups could play a more significant role in their Raman spectra.

2.2 Long range magnetic ordering

To probe the long-range magnetic ordering, superconducting quantum interference device vibrating sample magnetometer (SQUID-VSM) measurements were carried out. In the case of annite and biotite, single crystals were probed and the external magnetic field was applied perpendicular with respect to their basal planes. In the case of minnesotaite, a polycrystalline sample was measured and therefore the grains had random orientation with respect to the externally applied fields, effectively integrating over both in- and out-of-plane components.

Field cooling (FC) and zero field cooling (ZFC) M(T) curves were recorded starting from 400 K to 2 K. The critical ordering temperatures were determined from the global minima of the FC measurements first derivate dM(T)/dT. Figure 4 summarizes the VSM-SQUID results. The M(T) curves indicate the transition from (super)paramagnetic to ferrimagnetic in case of minnesotaite and annite, and anti-ferromagnetic in case of biotite. The transition temperatures considering the dM/dT curves and are 38.7 K for minnesotaite, 36.1 K for annite, and 4.9 K for biotite, as presented in the insets of Figures 4(c,f,i).

Magnetization loops M(H) were measured with the external field strength varied between ±6 T, at room temperature and below the critical ordering temperature. The results are presented in Figure 4a,d,g for minnesotaite, annite, and biotite, respectively. In contrast to annite and biotite, which are paramagnetic at 300 K, minnesotaite exhibits a clear saturation of the magnetization, a signature of superparamagnetism. A similar behaviour was observed in the case of iron-rich talc.[61] The field dependent magnetization for minnesotaite at low temperatures displays the ferromagnetic M(H) loop and reaches saturation at around 1.5 T (see Fig. 4a). For minnesotaite, the saturation magnetization of (0.7 ± 0.4) emu/g at 10 K was observed with a coercivity of 200 mT which is in good agreement with the values reported in the literature.[76]

For annite and biotite samples, the temperature dependent magnetic susceptibility ($\chi(T)$) was estimated from two FC M(T) curves with different applied external fields (see methods for details). The inverse of the estimated $\chi(T)$ in the paramagnetic regime is presented along with FC and ZFC M(T) curves in Figure 4e,h. The Curie-Weiss fit of the susceptibility in the high-temperature range provides a consistent estimate of the local moment per Fe ion between 4 and 5 μ_B, suggesting that both compounds contain mixtures of Fe^{2+} and Fe^{3+} ions. A more detailed fit was performed by assuming that the paramagnetic response originates from a mixture of Fe^{2+}/Fe^{3+} ions, which is expected in sheet silicates.[77] The fit can be described by the expression:

$$\chi(T) = \chi_0 + \frac{(1-p)C_1 + pC_2}{T - \theta} \tag{1}$$

with $C_1 = \eta_{Fe}\mu_B^2 g_1^2 S_1(S_1 + 1)/3\, k_B$, $C_2 = \eta_{Fe}\mu_B^2 g_2^2 S_2(S_2 + 1)/3\, k_B$, where g_1, S_1 and g_2, S_2 correspond to the Landé factor and spin quantum number of Fe^{2+} and Fe^{3+}, respectively; η_{Fe} denotes the average number of the octahedral sites occupied by Fe ions; θ is the paramagnetic Curie temperature for Fe^{3+} ions; χ_0 is the temperature independent susceptibility (containing the background and the van Vleck paramagnetism) and p represent the fraction of Fe^{3+} relative to the total amount of iron . Setting $g_1 = g_2 = 2$ (which is a reasonable assumption at least for the annite and biotite samples because the field is orthogonal to the easy plane of magnetization), $S_1 = 2$, $S_2 = 5/2$, partial Curie constants are found to be: $C_1 = 9.54 \cdot \eta_{Fe}$ K emu mol^{-1}, $C_2 = 13.92 \cdot \eta_{Fe}$ K emu mol^{-1}.

Fitting the susceptibility above the ordering temperature to the equation (1), we obtain a Fe^{2+}/Fe^{3+} ratio of 78/22 for annite and 53/47 for biotite, which is consistent with previous studies of Fe-rich sheet silicates.[77,78] In the case of minnesotaite, a more complex temperature dependence of the M(T) curves was observed (see Fig. 4b).
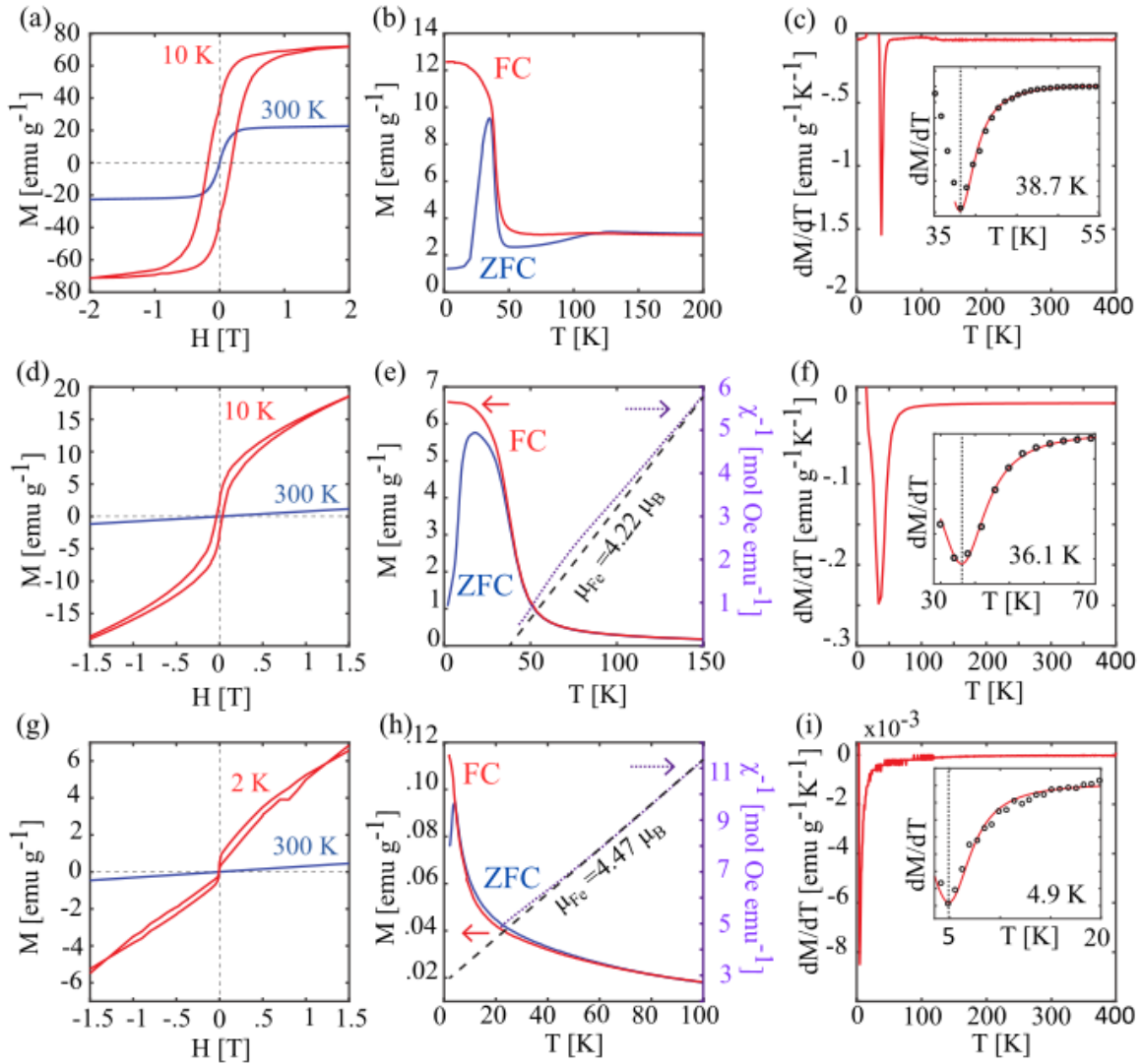
Figure 4: (a,b) M(H) loop and FC-ZFC M(T) curves for minnesotaite. (d,e) M(H) loop and FC-ZFC M(T) curves for annite, and (g,h) for biotite. All magnetic moments are scaled with respect to the mass of the measured samples. (c,f,i) dM/dT curves for minnesotaite, annite, and biotite, respectively, with insets focusing on the global minima and denoting the corresponding critical ordering temperatures. Mind that in the M(T) curves (b,e,h) the temperature scales are not the same, but rather focus on the regions near the transitions.

The paramagnetic Curie temperature, $\theta = 40$ K, for annite reveals the dominance of ferromagnetic interactions between Fe ions. However, for biotite $\theta = -27$ K was obtained, highlighting predominantly antiferromagnetic interactions and also a large degree of frustration, as $\theta/T_c \gg 1$. This behaviour can be attributed to the Fe/Mg disorder on the octahedral sublattice. Overall, the trends in the magnetic ordering tendency are consistent with the composition of the samples.

2.3 Incorporation of Fe in the phyllosilicates

To probe the oxidation state of iron in the phyllosilicate matrices, X-ray photoelectron spectroscopy (XPS) and X-ray absorption spectroscopy (XAS) were performed. The XPS/XAS spectra of iron compounds considerably differs depending on the ion oxidation state and the spin configuration.[79,80] In particular, the oxidation states of iron can be distinguished as Fe^{3+} (always high spin) and Fe^{2+} (can be high spin and low spin) by the binding energies of the Fe2p core-level peaks and their satellites in
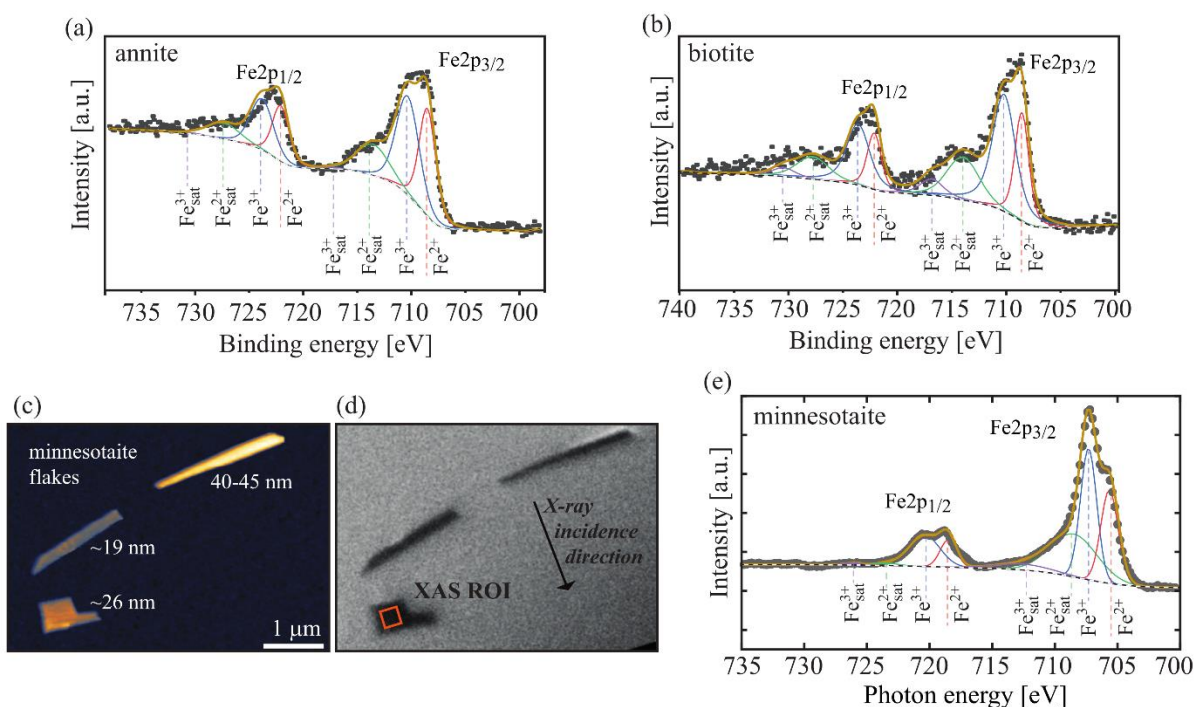
Figure 5: (a,b) XPS spectra of annite and biotite, (c) AFM image of minnesotaite flakes with their thickness (d) PEEM Image of minnesotaite flakes obtained during XAS measurements across the Fe $L_{3,2}$-edge. Squared orange box indicates the region from which the XAS spectrum represented in (e) has been obtained for minnesotaite.

the spectra. According to the theory, high-spin Fe^{2+} and Fe^{3+} configurations are multiplets due to spin-orbit and crystal field interactions, which can be described by the Gupta and Sen (GS) model.[81] Satellite peaks are generally characteristic of high-spin configurations due to the energy loss of photoelectrons on spin interactions.[82] Iron states in silicates are analysed by a simplified model, considering core levels and their satellites as singlet peaks with binding energies for Fe^{3+} typically 2-3 eV higher than for Fe^{2+}.[83]

XPS was applied to annite and biotite single crystals as large-enough (about 1 mm in diameter) crystalline samples with no inclusions were available (see methods for the details on sample preparation for XPS). The Fe2p spectra of annite and biotite are shown in Figure 5(a,b). Considering the simplified model, annite possesses Fe^{2+} in high spin configuration which is perceptible from the satellite peak of the correspondent multiplet. However, high-spin Fe^{3+} is not so unambiguous to deconvolute, since the Fe^{3+} satellites either have very low intensities or are hidden under the Fe2p$_{1/2}$ peak. Similar to annite, in the case of biotite a mixture of Fe^{2+} and Fe^{3+} states in high spin configuration was observed. According to the model, the Fe^{2+}/Fe^{3+} ratio is 45/55 and 35/65 for annite and biotite, respectively. The values obtained reveal a larger fraction of Fe^{3+} ions than what is obtained from the Currie-Weiss fit of the inverse $\chi(T)$, although exactly the same crystals used for the SQUID magnetometry measurements were also used to record the XPS spectra. The magnetization measurements probe the entire volume of the sample, while the photoelectrons are obtained from the surface. The observed discrepancy in the Fe^{2+}/Fe^{3+} ratio can be introduced by a possible surface-related defects. However, both techniques reveal a mixture of Fe^{2+} and Fe^3 ions, while in the perfectly ordered lattice only the Fe^{2+} should be present as suggested by the *ab inito* calculations.

Considering the polycrystallinity of minnesotaite, in order to avoid the influence of potential contaminants XAS imaging across the Fe $L_{3,2}$-edge for minnesotaite was measured on exfoliated single crystal flakes by means of x-ray photoemission electron microscopy (PEEM). The measurements were carried out on multilayer 2D flakes of minnesotaite transferred onto gold-coated Si chips. Upon illumination of the samples, the absorbed fraction of the X-rays leads to the excitation of inner shell electrons and a cascade of secondary electrons, which are measured by the microscope as a function of the incoming X-ray photon energy. The absorption spectra indicate the partial occupation of Fe^{2+} in a high-spin

configuration, which is evident from the satellite peaks. The same analysis procedure was applied as for the XPS spectra of annite and biotite, estimating Fe^{2+}/Fe^{3+} ratio for minnesotaite of 54/46.

Discussion

Phyllosilicates provide a natural solution of ambient stability for 2D intrinsic magnetism and can thus potentially represent a robust platform for future technological advancements and next generation data storage devices. Here we demonstrated that the magnetic ordering in naturally occurring iron rich phyllosilicates showing 2:1 layering (minnesotaite, annite, and biotite) persists down to few monolayers. An important question that remains to be answered is how to tune the critical temperature and whether it is possible to significantly increase it.

A trend can be drawn from our results in conjunction with previously published data on bulk crystals. Figure 6 shows the magnetic ordering (the Curie temperature), measured for several classes of Fe-rich phyllosilicates, all having the same octahedral sheet as the main functional unit.[59,76,77,84,85] The magnetic behaviour of all these compounds is similar and can be rationalized in terms of the local electronic structure of Fe^{2+} and Fe^{3+} ions.[77,85] Specifically, the ground state magnetic structure can be described as ferromagnetically ordered layers of in-plane oriented magnetic moment of iron, with dipolar interactions in weakly coupling adjacent layers antiferromagnetically in a perfectly ordered case. Reducing the fraction of Fe or increasing the ratio of Fe^{3+}/Fe^{2+} ions results in stronger disorder within the planes, which eventually destroys ordering and silicates with low Fe content exhibit a complex temperature dependence of the susceptibility akin to that of spin glasses.[86] An important point of this picture is that it suggests the ordering temperature of Fe-rich silicates is determined practically only by exchange interactions between iron ions within individual layers. The effective strength of the exchange interaction is directly related to the paramagnetic Curie temperature, θ, extracted from the temperature dependent susceptibility. Thus, by examining values of θ we can understand the magnetic behaviour of individual octahedral sheets themselves.
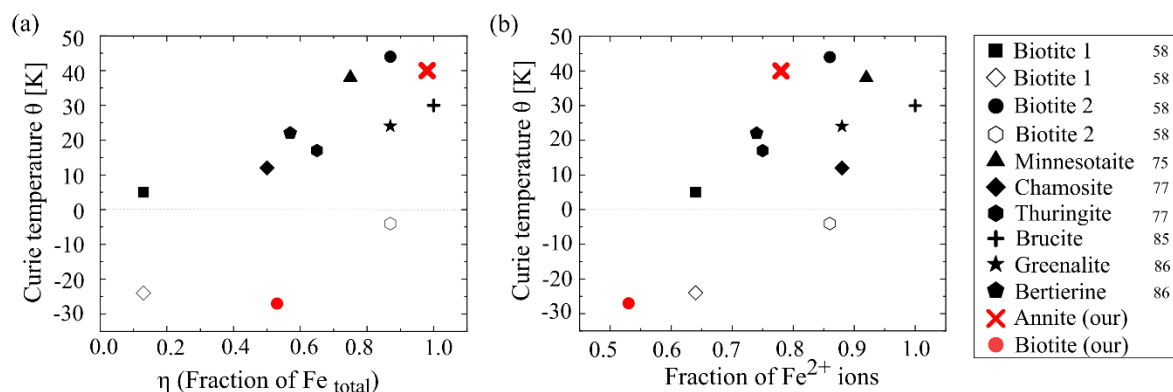

Figure 6: The paramagnetic Curie temperature, θ, as a function of (a) fraction of total Fe ions and (b) fraction of Fe-occupied sites by Fe^{2+} ions, in all cases considering the central sites of the octahedral sheet for various phyllosilicates. Most of the data is presented for polycrystalline samples, for which only an effective θ can be extracted. For monocrystalline samples (Ref. [58] and this work) filled symbols correspond to $\theta_\perp$, where the susceptibility is measured for the magnetic field parallel to the c-axis, while empty symbols correspond to $\theta_\parallel$ for the field orthogonal to the c-axis.

Considering Figure 6, θ depends on the total fraction of Fe ions in the octahedral sheets (Fig. 6(a)). When considering the samples with dominant ferromagnetic interactions ($\theta > 0$), simply a higher amount of Fe substitution leads to higher θ. Supposing that there are only Fe^{2+} ions we should expect that the maximum of θ is observed at the maximum fraction of iron ions equal to 1. However, summarizing results on magnetic measurements for various phyllosilicates with respect also to the Fe oxidation states (Fig. 6(b)), we see that this is not the case. Despite a certain scatter of results (caused by differences in samples, measurements, possible impurities, etc.), there is a clear trend that the Curie temperature increases with increasing fraction of Fe^{2+}. However, the observed maximum is located around 75-90 %. It is important to keep in mind that the remaining 10-25 % of metallic ions are not just Mg or Al but these

sites are occupied by Fe^{3+} ions. The effect of adding Fe^{3+} ions to a primarily Fe^{2+}-occupied sublattice is two-fold. On the one hand, Fe^{3+} ions, with their d^5 configuration do not contribute to the magnetocrystalline anisotropy, thus reducing the tendency to 2D magnetic ordering. On the other hand, Fe^{3+} introduces two new types of exchange interaction types, namely Fe^{3+}-Fe^{2+} and Fe^{3+}-Fe^{3+} interactions. We have estimated NN interactions by performing total energy calculations in an idealized Fe-brucite-like structure (see Methods) and obtained the following values of the interactions (positive meaning ferromagnetic): $J_{2+2+} = 5.7$ meV, $J_{3+2+} \approx 6J_{2+2+}$, and $J_{3+3+} = -0.5J_{2+2+}$. These interactions are consistent with the Goodenough-Kanamori rules and show that Fe^{3+} actually enhances ferromagnetic interactions when it is surrounded only by Fe^{2+} ions.[87] This implies that a small amount of Fe^{3+} distributed randomly over the Fe sublattice can increase the value of θ, which could be the origin behind the position of the maximum θ as a function of Fe^{2+} ion fraction. Note that the higher fraction of Fe^{3+} ions will produce more and more Fe^{3+}-Fe^{3+} pairs with anti-ferromagnetic type of interactions, which will result in a reduction of θ and magnetic frustration, which can also explain the spin-glass-like behavior of phyllosilicates with lower Fe content.

Conclusions

Our study addresses the relation between the structure and the magnetic properties of iron-rich phyllosilicates, magnetic minerals that can be thinned down to their monolayers using a mechanical exfoliation process. We studied three mineral specimens, the rare talc-like mineral minnesotaite, and the micas annite, as well as more commonly occuring biotite. All three species can be exfoliated down to few monolayers, and their thin-film samples were found to be fully air stable. However, in the case of minnesotaite, peculiar structural changes can occur, producing complex incommensurate patterns and favouring defect formation.[67]

Magnetic measurements show that all three materials exhibit antiferromagnetic or ferrimagnetic ordering at temperatures below 40 K. The analysis of the temperature dependent susceptibility reveals that annite has a positive value of the paramagnetic Curie temperature, implying the dominance of ferromagnetic exchange interactions. On the other hand, biotite, with similar structure as annite has a lower Fe content and a higher fraction of Fe^{3+} ions, all contributing to a negative Curie temperature. This implies predominantly antiferromagnetic interactions and also a large degree of frustration.

The character of interactions can be traced back to both the overall fraction of Fe in the metallic positions of the octahedral sheet and to the relative fraction of Fe^{3+} ions with respect to Fe^{2+} ions. The effect of Fe^{3+} is two-fold, enhancing ferromagnetic interactions mediated by Fe^{2+}-Fe^{3+} pairs, and reducing the crystalline anisotropy and forming Fe^{3+}-Fe^{3+} pairs which have a detrimental effect on the in-plane ferromagnetic ordering. This behaviour is supported by *ab-initio* estimates of nearest-neighbour magnetic exchange interactions. This is also supported by our meta-study and previously published results of magnetic phyllosilicates, which show that the highest Curie temperature is not achieved for the highest content of Fe^{2+} ions (achieved in Fe-brucite) but for compounds with about 10-25% of Fe^{2+} ions replaced by randomly distributed Fe^{3+} ions.

Methods

Sample preparation

The flakes of minnesotaite, annite and biotite were prepared by micromechanical exfoliation using sticky tape (Nitto Denko ELP BT150ECM). After multiple pealing against two pieces of the tape, the material was deposited on SiO_2/Si chips (300 nm oxide layer), gold-coated Si chips, or cleaved graphite crystals, via PDMS. After slowly peeling off the PDMS, flakes with different thicknesses were identified with the help of an optical microscope.

SQUID magnetometry

Long range magnetic ordering was measure using superconducting quantum interference device - vibrating sample magnetometer (SQUID-VSM) MPMS2 from Quantum Design. Bulk crystals were placed inside a plastic straw holder and inserted into the electromagnet. All the magnetization curves

were normalized to the diamagnetism of substrate and the values of magnetic moment was normalized to the mass of the measured crystals. M(T) measurements in the FC case were done with two different externally applied fields. For the minnesotaite and biotite samples external fields of 5 mT and 20 mT were applied while 10 mT and 100 mT were applied for the annite sample. The susceptibility was estimated from the two FC M(T) curves by a simple linear approximation considering the M(H) point of origin as the third and fixed point. The results are consistent with the susceptibility obtained from the derivates of M(H) loops in the paramagnetic regime (at 45 K and 300 K). The scaling of the susceptibility was done considering the molar mass of annite to be 1032.8 g·mol^{-1}, and 921.94 g·mol^{-1} for biotite. Curie-Weiss fit of the susceptibility was applied in a 100 – 400 K range for annite and 50 – 400 K range for biotite.

Structural characterization

Element mapping and quantitative analysis was performed using the Jeol JXA8200 electron probe microanalyzer at the Chair of Resource Mineralogy at Montanuniversität Leoben. Investigations were carried out in WDS mode with counting time ranging from 10 s to 300 s. Other operational parameters include 10-100 nA beam currents and analysing voltages of 10-15 KV. Ka lines of Si, Al, Mg and Fe were used for analysis. ZAF corrections was applied and kaersutite and magnetite were used as standards for calibration.

X-ray photoelectron spectroscopy

X-ray photoelectron spectrometer ESCALAB 250Xi was used to determine the oxidation state of iron. Bulk crystals were were used in the experiments. Spectra were acquired with monochromated Al Ka excitation (hv = 1486.7 eV) at pass energy of 20 eV providing a spectral resolution of 0.5 eV. No external charge compensation was used, instead the charging effect was corrected to the Si_{2p} peaks (101.6 eV) assuming their chemical states in the studied silicates to be same. Spectra was acquired and processed using the Advantage software.

X-ray absorption spectroscopy

X-ray Absorption spectroscopy was performed using the scanning photoemission electron microscope at the UE49-PGM SPEEM beamline of BESSY II. 2D flakes of minnesotaite were transferred on gold-coated Si chips. Images and spectra were recorded using linear polarized X-rays at a sample temperature of 40 K.

Raman spectroscopy

Raman features of the samples were recorded using Horiba LabRam HR evolution confocal Raman spectrometer. Thick flakes (between 20 nm and 200 nm) of the minerals were transferred on HOPG. The measurements were carried out with 532.1 nm laser (1800 gr/mm and 100 mW power on the sample surface), and 100x magnification lens. No sample degradation/damage was noticed after continuous illumination under the laser beam.

AFM and MFM measurements

Topography analysis (using AFM) and local magnetic moment measurements (using MFM) were carried out on Horiba-AIST-NT Omegascope system at room temperature. For topography analysis, non-ferromagnetic PtIr-coated Electrical Force Microscopy (EFM) probes of type ACCESS-EFM from AppNano (~ 30 nm tip curvature radius, ~ 63 kHz resonance, ~ 2.7 Nm^{-1} force constant) were used. MFM signals were recorded using TipsNano MFM01 probes with CoCr coating (~40 nm tip curvature radius, ~70 kHz resonance, ~5 N/m force constant). Prior to MFM measurements, counter check of probes magnetic response were carried out on a magnetic hard drive (MFM test samples). The probes were subjected to out-of-plane magnetic field with flux density of 200 mT for around 30 minutes prior to MFM experiments. In field measurements were performed on a "home-built" sample holder with permanent magnet of 180 mT, estimated at the sample surface. Hall probe (M-test MK4, Maurer Magnetic AG) was used to confirm the flux density of externally applied magnetic field. MFM signals were recorded in a two-pass regime, with second-pass lift height of 20 nm. MFM phase and AFM topography were mapped and processed via Gwydion v2.55 (an open source software for SPM analysis).

DFT calculation

DFT calculations were performed using the projector augmented waves[88] method as implemented in the Vienna Ab-initio Simulation Package.[89–91] Generalized gradient approximation with the Perdew-Burke-Ernzerhof parameterization for solid was employed as an exchange-correlation functional, as it was shown to give the best-relaxed structure for talc.[92,93] Furthermore, we use the value $U_{eff} = 4$ eV within the DFT+U rotationally invariant scheme [94] to better describe localized states of Fe ions. Atomic positions were relaxed to the accuracy in forces of 0.01 eVÅ^{-1}. To estimate nearest-neighbour magnetic exchange interactions we construct a model system, representing a $4 \times 2\sqrt{3}$ supercell based on the brucite unit cell, with a pair of adjacent metallic sites occupied by Fe. Naturally, this structure contains only Fe2+ ions. Ions with 3+ states are introduced by removing a hydrogen atom next the target site. The magnetic exchange interaction is evaluated as $(E_{\uparrow\downarrow} - E_{\uparrow\uparrow})/2$, corresponding to a Heisenberg-type Hamiltonian $H = -\sum_{<ij>} J S_i \cdot S_j$. Here, $E_{\uparrow\downarrow}$, $E_{\uparrow\uparrow}$ denote energies of, respectively, anti-parallel and parallel spin configurations for the pair of Fe ions. We have also checked the dependence of the obtained interactions on U_{eff} and the degree of trigonal distortion of oxygen octahedra. Both of these factors can significantly affect the absolute values of the interactions but do not change the signs, the ratios of magnitudes remaining similar to the one given in the main text. The values given in the main text correspond to zero trigonal distortion and $U_{eff} = 4$ eV.

Conflict of Interest

The authors declare no conflict of interest.

Author Contributions

M.Z.K. with assistance of A.M. carried out the sample preparation, AFM, and MFM characterization, and with M.A.A. carried out Raman spectroscopy measurements. M.Z.K. with C.T. interpreted AFM and MFM data. O.P. carried out the calculations. M.Z. with support of J.R. performed EPMA/WDS characterization, and WDS data interpretation. A.S. carried out SQUID experiments, and with G.S. interpreted SQUID data. O.S. performed XPS measurements, and with help of G.S. and D.R.T.Z. interpreted the data. M.Z.K. under supervision of S.V. and F.K. performed XAS experiments M.Z.K compiled all the data. M.Z.K., A.M. and O.P. wrote the manuscript. All authors discussed the results and reviewed the manuscript.

References:

1. Novoselov KS, Geim AK, Morozov SV, Jiang DE, Zhang Y, Dubonos SV, Grigorieva IV, Firsov AA. *Electric field effect in atomically thin carbon films*. Science **306**, 666, 2004.

2. Gupta A, Sakthivel T, Seal S. *Recent development in 2D materials beyond graphene*. Progress in Materials Science **73**, 44, 2015.

3. Han W, Kawakami RK, Gmitra M, Fabian J. *Graphene spintronics*. Nature Nanotechnology **9**, 794, 2014.

4. Ahn EC. *2D materials for spintronic devices*. npj 2D Materials and Applications **4**, 17, 2020.

5. Ge J, Luo T, Lin Z, Shi J, Liu Y, Wang P, Zhang Y, Duan W, Wang J. *Magnetic moments induced by atomic vacancies in transition metal dichalcogenide flakes*. Advanced Materials **33**, 2005465, 2021.

6. Yazyev OV, Helm L. *Defect-induced magnetism in graphene*. Physical Review B **75**, 125408, 2007.

7. Avsar A, Ciarrocchi A, Pizzochero M, Unuchek D, Yazyev OV, Kis A. *Defect induced, layer-modulated magnetism in ultrathin metallic PtSe$_2$*. Nature Nanotechnology **14**, 674, 2019.

8. Klimovskikh II, Otrokov MM, Estyunin D, Eremeev SV, Filnov SO, Koroleva A, Shevchenko E, Voroshnin V, Rybkin AG, Rusinov IP, Blanco-Rey M. *Tunable 3D/2D magnetism in the (MnBi$_2$Te$_4$)(Bi$_2$Te$_3$) m topological insulators family*. npj Quantum Materials **5**, 54, 2020.

9. Jiang S, Li L, Wang Z, Mak KF, Shan J. *Controlling magnetism in 2D CrI$_3$ by electrostatic doping*. Nature Nanotechnology **13**, 549, 2018.

10. Chen R, Luo F, Liu Y, Song Y, Dong Y, Wu S, Cao J, Yang F, N'Diaye A, Shafer P, Liu Y. *Tunable room-temperature ferromagnetism in Co-doped two-dimensional van der Waals ZnO*. Nature Communications **12**, 3952, 2021.

11. Li H, Ruan S, Zeng YJ. *Intrinsic van der Waals magnetic materials from bulk to the 2D limit: new frontiers of spintronics*. Advanced Materials **31**, 1900065, 2019.

12. Mak KF, Shan J, Ralph DC. *Probing and controlling magnetic states in 2D layered magnetic materials*. Nature Reviews Physics **1**, 646, 2019.

13. Tomar S, Ghosh B, Mardanya S, Rastogi P, Bhadoria BS, Chauhan YS, Agarwal A, Bhowmick S. *Intrinsic magnetism in monolayer transition metal trihalides: A comparative study*. Journal of Magnetism and Magnetic Materials **489**, 165384, 2019.

14. Lee JU, Lee S, Ryoo JH, Kang S, Kim TY, Kim P, Park CH, Park JG, Cheong H. *Ising-type magnetic ordering in atomically thin FePS$_3$*. Nano Letters **16**, 7433, 2016.

15. Huang B, Clark G, Navarro-Moratalla E, Klein DR, Cheng R, Seyler KL, Zhong D, Schmidgall E, McGuire MA, Cobden DH, Yao W. *Layer-dependent ferromagnetism in a van der Waals crystal down to the monolayer limit*. Nature **546**, 270, 2017.

16. Gong C, Li L, Li Z, Ji H, Stern A, Xia Y, Cao T, Bao W, Wang C, Wang Y, Qiu ZQ. *Discovery of intrinsic ferromagnetism in two-dimensional van der Waals crystals*. Nature **546**, 265, 2017.

17. May AF, Ovchinnikov D, Zheng Q, Hermann R, Calder S, Huang B, Fei Z, Liu Y, Xu X, McGuire MA. *Ferromagnetism near room temperature in the cleavable van der Waals crystal Fe$_5$GeTe$_2$*. ACS Nano **13**, 4436, 2019.

18. Telford EJ, Dismukes AH, Dudley RL, Wiscons RA, Lee K, Chica DG, Ziebel ME, Han MG, Yu J, Shabani S, Scheie A. *Coupling between magnetic order and charge transport in a two-dimensional magnetic semiconductor*. Nature Materials **21**, 754, 2022.

19.   Huang B, Clark G, Klein DR, MacNeill D, Navarro-Moratalla E, Seyler KL, Wilson N, McGuire MA, Cobden DH, Xiao D, Yao W. *Electrical control of 2D magnetism in bilayer CrI_3*. Nature Nanotechnology **13**, 544, 2018.

20.   Chu YH, Martin LW, Holcomb MB, Gajek M, Han SJ, He Q, Balke N, Yang CH, Lee D, Hu W, Zhan Q. *Electric-field control of local ferromagnetism using a magnetoelectric multiferroic*. Nature Materials **7**, 478, 2008.

21.   Liu Y, Shao Q. *Two-dimensional materials for energy-efficient spin–orbit torque devices*. ACS Nano **14**, 9389, 2020.

22.   Klein DR, MacNeill D, Lado JL, Soriano D, Navarro-Moratalla E, Watanabe K, Taniguchi T, Manni S, Canfield P, Fernández-Rossier J, Jarillo-Herrero P. *Probing magnetism in 2D van der Waals crystalline insulators via electron tunneling*. Science **360**, 1218, 2018.

23.   Peters LC, Christianen PC, Engelkamp H, Groenenboom GC, Maan JC, Kampert E, Tinnemans PT, Rowan AE, Zeitler U. *Magnetic anisotropy of individually addressed spin states*. Physical Review Research **3**, L042042, 2021.

24.   Bacaksiz C, Šabani D, Menezes RM, Milošević MV. *Distinctive magnetic properties of CrI_3 and $CrBr_3$ monolayers caused by spin-orbit coupling*. Physical Review B **103**, 125418, 2021.

25.   Ashcroft NW, Mermin ND. Solid state physics. Cengage Learning, 2022.

26.   Jena AK, Mallik SK, Sahu MC, Sahoo S, Sahoo AK, Sharma NK, Mohanty J, Gupta SK, Ahuja R, Sahoo S. *Strain-mediated ferromagnetism and low-field magnetic reversal in Co doped monolayer WS_2 /WS_2*. Scientific Reports **12**, 1, 2022.

27.   Siegrist F, Gessner JA, Ossiander M, Denker C, Chang YP, Schröder MC, Guggenmos A, Cui Y, Walowski J, Martens U, Dewhurst JK. *Light-wave dynamic control of magnetism*. Nature **571**, 240, 2019.

28.   Li D, Li S, Zhong C, He J. *Tuning magnetism at the two-dimensional limit: A theoretical perspective.* Nanoscale **13**, 19812, 2021.

29.   Xie H, Luo X, Ye G, Ye Z, Ge H, Sung SH, Rennich E, Yan S, Fu Y, Tian S, Lei H. *Twist engineering of the two-dimensional magnetism in double bilayer chromium triiodide homostructures*. Nature Physics **18**, 30, 2022.

30.   Gibertini M, Koperski M, Morpurgo AF, Novoselov KS. *Magnetic 2D materials and heterostructures*. Nature Nanotechnology **14**, 408, 2019.

31.   Zhang F, Zheng B, Sebastian A, Olson DH, Liu M, Fujisawa K, Pham YT, Jimenez VO, Kalappattil V, Miao L, Zhang T. *Monolayer vanadium-doped tungsten disulfide: a room-temperature dilute magnetic semiconductor*. Advanced Science **7**, 001174, 2020.

32.   Fu S, Kang K, Shayan K, Yoshimura A, Dadras S, Wang X, Zhang L, Chen S, Liu N, Jindal A, Li X. *Enabling room temperature ferromagnetism in monolayer MoS_2 via in situ iron-doping*. Nature Communications **11**, 2034, 2020.

33.   Wang Y, Li S, Yi J. *Electronic and magnetic properties of Co doped MoS_2 monolayer.* Scientific Reports. **6**, 24153, 2016.

34.   Khan MJ, Liu J, Latif A, Majeed I, Ullah H, Asghar M, Ahmad J. *Investigating structural, electronic, magnetic, and optical properties of Co-doped and Co-X (X= Fe, Mn) co-doped MoS_2 for optoelectronic applications*. Journal of Molecular Modeling **28**, 310, 2022.

35.   Deng J, Zhou Z, Chen J, Cheng Z, Liu J, Wang Z. *Vanadium-Doped Molybdenum Diselenide Atomic Layers with Room-Temperature Ferromagnetism*. ChemPhysChem **23**, e202200162, 2022.

36. Tiwari S, Van de Put ML, Sorée B, Vandenberghe WG. *Magnetic order and critical temperature of substitutionally doped transition metal dichalcogenide monolayers*. npj 2D Materials and Applications **5**, 54, 2021.

37. Frisenda R, Niu Y, Gant P, Muñoz M, Castellanos-Gomez A. *Naturally occurring van der Waals materials. npj 2D Materials and Applications* **4**, 38, 2020.

38. Cadore AR, de Oliveira R, Longuinhos R, de C Teixeira V, Nagaoka DA, Alvarenga VT, Ribeiro-Soares J, Watanabe K, Taniguchi T, Paniago RM, Malachias A. *Exploring the structural and optoelectronic properties of natural insulating phlogopite in van der Waals heterostructures*. 2D Materials **9**, 035007, 2022.

39. Santos JC, Barboza AP, Matos MJ, Barcelos ID, Fernandes TF, Soares EA, Moreira RL, Neves BR. *Exfoliation and characterization of a two-dimensional serpentine-based material*. Nanotechnology **30**, 445705, 2019.

40. Mahapatra PL, Singh AK, Tromer R, Karthik R, Ambresha M, Costin G, Lahiri B, Kundu TK, Ajayan PM, Altman EI, Galvao DS. *Energy harvesting using two-dimensional (2D) d-silicates from abundant natural minerals*. Journal of Materials Chemistry C **11**, 2098, 2023.

41. de Oliveira R, Guallichico LA, Policarpo E, Cadore AR, Freitas RO, da Silva FM, Teixeira VD, Paniago RM, Chacham H, Matos MJ, Malachias A. *High throughput investigation of an emergent and naturally abundant 2D material: Clinochlore.* Applied Surface Science **599**, 153959, 2022.

42. Huang Z, Lan T, Dai L, Zhao X, Wang Z, Zhang Z, Li B, Li J, Liu J, Ding B, Geim AK. *2D Functional Minerals as Sustainable Materials for Magneto-Optics.* Advanced Materials **34**, 2110464, 2022.

43. Ji X, Ge L, Liu C, Tang Z, Xiao Y, Chen W, Lei Z, Gao W, Blake S, De D, Shi B. *Capturing functional two-dimensional nanosheets from sandwich-structure vermiculite for cancer theranostics*. Nature Communications, **12**, 1124, 2021.

44. Castellanos-Gomez A, Wojtaszek M, Tombros N, Agraït N, van Wees BJ, Rubio-Bollinger G. *Atomically thin mica flakes and their application as ultrathin insulating substrates for graphene.* Small **7**, 2491, 2011.

45. Vasić B, Gajić R, Milošević I, Medić Ž, Blagojev M, Opačić M, Kremenović A, Lazić D. *Natural two-dimensional pyrophyllite: Nanoscale lubricant, electrical insulator and easily-machinable material.* Applied Surface Science **608**, 155114, 2023.

46. Franceschi G, Kocán P, Conti A, Brandstetter S, Balajka J, Sokolović I, Valtiner M, Mittendorfer F, Schmid M, Setvín M, Diebold U. *Resolving the intrinsic short-range ordering of K+ ions on cleaved muscovite mica.* Nature Communications **14**, 208, 2023.

47. Longuinhos R, Cadore AR, Bechtel HA, JS De Matos C, Freitas RO, Ribeiro-Soares J, Barcelos ID. *Raman and Far-Infrared Synchrotron Nanospectroscopy of Layered Crystalline Talc: Vibrational Properties, Interlayer Coupling, and Symmetry Crossover*. The Journal of Physical Chemistry C **27**, 5876, 2023.

48. Wang QH, Bedoya-Pinto A, Blei M, Dismukes AH, Hamo A, Jenkins S, Koperski M, Liu Y, Sun QC, Telford EJ, Kim HH. *The magnetic genome of two-dimensional van der Waals materials*. ACS Nano **16**, 6960, 2022.

49. Vasić B, Czibula C, Kratzer M, Neves BR, Matković A, Teichert C. *Two-dimensional talc as a van der Waals material for solid lubrication at the nanoscale.* Nanotechnology **32**, 265701, 2021.

50. Alencar AB, Barboza AP, Archanjo BS, Chacham H, Neves BR. *Experimental and theoretical investigations of monolayer and few-layer talc*. 2D Materials **2**, 015004, 2015.

51. Batista AB, Stanley M, de Brito AC, Vasconcellos R, Munk M, José-Bueno M, Godoy C, de Alvarenga ÉC, de Vasconcelos CK, Righi A, de Sousa EM. *Improved bioceramic coatings reinforced by nanostructured talc.* Surface and Coatings Technology **441**, 128589, 2022.

52. Nutting D, Prando GA, Severijnen M, Barcelos ID, Guo S, Christianen PC, Zeitler U, Gobato YG, Withers F. *Electrical and optical properties of transition metal dichalcogenides on talc dielectrics.* Nanoscale **13**, 15853, 2021.

53. Maruvada A, Shubhakar K, Raghavan N, Pey KL, O'Shea SJ. *Dielectric breakdown of 2D muscovite mica.* Scientific Reports **12**, 1, 2022.

54. Arora A, Ganapathi KL, Dixit T, Miryala M, Masato M, Rao MR, Krishnan A. *Thickness-Dependent Nonlinear Electrical Conductivity of Few-Layer Muscovite Mica.* Physical Review Applied, **17**, 064042, 2022.

55. Zhang R, Sun Y, Chen W, Zhao S, Wang J, Teng C, Liu B, Cheng HM. *Switchable and Reversible p+/n+ Doping in 2D Semiconductors by Ionic 2D Minerals.* Advanced Functional Materials, 2213809, 2023.

56. Yang Z, Wang D, Wang S, Tan C, Yang L, Wang Z. *Electrically Tuning Interfacial Ion Redistribution for mica/WSe2 Memory Transistor.* Advanced Electronic Materials **9**, 2200679, 2023.

57. Niu Y, Villalva J, Frisenda R, Sanchez-Santolino G, Ruiz-González L, Pérez EM, García-Hernández M, Burzurí E, Castellanos-Gomez A. *Mechanical and liquid phase exfoliation of cylindrite: a natural van der Waals superlattice with intrinsic magnetic interactions.* 2D Materials **6**, 035023, 2019.

58. Zou YC, Mogg L, Clark N, Bacaksiz C, Milovanovic S, Sreepal V, Hao GP, Wang YC, Hopkinson DG, Gorbachev R, Shaw S. *Ion exchange in atomically thin clays and micas.* Nature Materials **20**, 1677, 2021.

59. Ballet O, Coey JM. *Magnetic properties of sheet silicates; 2: 1 layer minerals.* Physics and Chemistry of Minerals **8**, 218, 1982.

60. Ma Z, Skumryev V, Gich M. *Magnetic properties of synthetic fluorophlogopite mica crystals.* Materials Advances **1**, 1464, 2020.

61. Matković A, Ludescher L, Peil OE, Sharma A, Gradwohl KP, Kratzer M, Zimmermann M, Genser J, Knez D, Fisslthaler E, Gammer C. *Iron-rich talc as air-stable platform for magnetic two-dimensional materials.* npj 2D Materials and Applications **5**, 94, 2021.

62. Bleam WF. *Atomic theories of phyllosilicates: Quantum chemistry, statistical mechanics, electrostatic theory, and crystal chemistry.* Reviews of Geophysics **31**, 51, 1993.

63. Mottana A, Sassi FP, Thompson JB, Guggenheim S, editors. *Micas: Crystal chemistry & metamorphic petrology.* Walter de Gruyter GmbH & Co KG, 2018.

64. Harrison TN. *Chemical variation in micas from the Cairngorm pluton, Scotland.* Mineralogical Magazine **54**, 355, 1990.

65. Liebau F. *Structural chemistry of silicates: structure, bonding, and classification.* Springer Science & Business Media, 2012.

66. Uhlig MR, Benaglia S, Thakkar R, Comer J, Garcia R. *Atomically resolved interfacial water structures on crystalline hydrophilic and hydrophobic surfaces.* Nanoscale **13**, 5275, 2021.

67. Guggenheim S, Eggleton RA. *Structural modulations in iron-rich and magnesium-rich minnesotaite.* The Canadian Mineralogist **24**, 479, 1986.

68.   Bailey SW, editor. *Hydrous phyllosilicates:(exclusive of micas)*. Walter de Gruyter GmbH & Co KG, 2018.

69.   Beausoleil N, Lavallee P, Yelon A, Ballet O, Coey JM. *Magnetic properties of biotite micas.* Journal of applied physics **54**, 906, 1983.

70.   Golla D, Chattrakun K, Watanabe K, Taniguchi T, LeRoy BJ, Sandhu A. *Optical thickness determination of hexagonal boron nitride flakes.* Applied Physics Letters **102**, 161906, 2013.

71.   Funke S, Wurstbauer U, Miller B, Matković A, Green A, Diebold A, Röling C, Thiesen PH. *Spectroscopic imaging ellipsometry for automated search of flakes of mono-and n-layers of 2D-materials.* Applied Surface Science **421**, 435, 2017.

72.   Gorbachev RV, Riaz I, Nair RR, Jalil R, Britnell L, Belle BD, Hill EW, Novoselov KS, Watanabe K, Taniguchi T, Geim AK. *Hunting for monolayer boron nitride: optical and Raman signatures.* Small **7**, 465, 2011.

73.   Tran TH, Rodriguez RD, Cheshev D, Villa NE, Aslam MA, Pešić J, Matković A, Sheremet E. *A universal substrate for the nanoscale investigation of two-dimensional materials.* Applied Surface Science **604**, 154585, 2022.

74.   Wang A, Freeman JJ, Jolliff BL. *Understanding the Raman spectral features of phyllosilicates.* Journal of Raman Spectroscopy **46**, 829, 2015.

75.   Nasdala L, Wenzel M, Andrut M, Wirth R, Blaum P. *The nature of radiohaloes in biotite: Experimental studies and modeling.* American Mineralogist. **86**, 498, 2001.

76.   Ballet O, Coey JM, Mangin P, Townsend MG. *Ferrous talc-a planar antiferromagnet.* Solid state communications **55**, 787, 1985.

77.   Ballet O, Coey JM, Burke KJ. *Magnetic properties of sheet silicates; 2: 1: 1 layer minerals.* Physics and Chemistry of Minerals **12**, 370, 1985.

78.   Guggenheim S, Eggleton RA. *Modulated 2: 1 layer silicates; review, systematics, and predictions.* American Mineralogist **72**, 724, 1987.

79.   Grosvenor AP, Kobe BA, Biesinger MC, McIntyre NS. *Investigation of multiplet splitting of Fe$_{2p}$ XPS spectra and bonding in iron compounds.* Surface and Interface Analysis: An International Journal devoted to the development and application of techniques for the analysis of surfaces, interfaces and thin films **36**, 1564, 2004.

80.   McIntyre NS, Zetaruk DG. *X-ray photoelectron spectroscopic studies of iron oxides*. Analytical Chemistry **49**, 1521, 1977.

81.   Gupta RP, Sen SK. *Calculation of multiplet structure of core p-vacancy levels*. Physical Review B **10**, 71, 1974.

82.   Seah MP. *The quantitative analysis of surfaces by XPS: A review. Surface and Interface Analysis* **2**, 222, 1980.

83.   Elmi C, Guggenheim S, Gieré R. *Surface crystal chemistry of phyllosilicates using X-ray photoelectron spectroscopy: A review*. Clays and Clay Minerals **64**, 537, 2016.

84.   Miyamoto H. *The magnetic properties of Fe(OH)$_2$.* Materials Research Bulletin **11**, 329, 1976.

85.   Coey JM, Ballet O, Moukarika A, Soubeyroux JL. *Magnetic properties of sheet silicates; 1: 1 layer minerals*. Physics and Chemistry of Minerals **7**, 141, 1981.

86.   Coey JM. *Magnetic properties of iron in soil iron oxides and clay minerals*. Iron in soils and clay minerals, 397, 1988.

87.   Goodenough JB. *Magnetism and the chemical bond.* Interscience Publishers, 1963.

88.   Blöchl PE. *Projector augmented-wave method.* Physical Review B **50**, 17953, 1994.

89.   Kresse G, Hafner J. *Ab initio molecular dynamics for liquid metals.* Physical Review B **47**, 558, 1993.

90.   Kresse G, Furthmüller J. *Efficient iterative schemes for ab initio total-energy calculations using a plane-wave basis set.* Physical Review B **54**, 11169, 1996.

91.   Kresse G, Joubert D. *From ultrasoft pseudopotentials to the projector augmented-wave method.* Physical Review B **59**, 1758, 1999.

92.   Perdew JP, Ruzsinszky A, Csonka GI, Vydrov OA, Scuseria GE, Constantin LA, Zhou X, Burke K. *Restoring the density-gradient expansion for exchange in solids and surfaces.* Physical Review Letters **100**, 136406, 2008.

93.   Tunega D, Bučko T, Zaoui A. *Assessment of ten DFT methods in predicting structures of sheet silicates: Importance of dispersion corrections.* The Journal of Chemical Physics **137**, 114105, 2012.

94.   Dudarev SL, Botton GA, Savrasov SY, Humphreys CJ, Sutton AP. *Electron-energy-loss spectra and the structural stability of nickel oxide: An LSDA+ U study.* Physical Review B **57**, 1505, 1998.